Cement and Concrete Research 146 (2021) 106476

Contents lists available at ScienceDirect

Cement and Concrete Research

journal homepage: www.elsevier.com/locate/cemconres

Plastic deformation mechanism of calcium-silicate hydrates determined by deviatoric-stress Raman spectroscopy

David W. Gardner [a], Jiaqi Li [b], Martin Kunz [c], Chenhui Zhu [c], Paulo J.M. Monteiro [b], Roya Maboudian [a], Carlo Carraro [a,*]

[a] Department of Chemical and Biomolecular Engineering, University of California, Berkeley, CA 94720, United States
[b] Department of Civil and Environmental Engineering, University of California, Berkeley, CA 94720, United States
[c] Advanced Light Source, Lawrence Berkeley National Laboratory, Berkeley, CA 94720, USA

ARTICLE INFO

Keywords:
Calcium-silicate-hydrate
Small-angle X-ray scattering
Spectroscopy
Creep
Carbonation

ABSTRACT

Creep of the cement matrix affects the structural stability of concrete. In Portland cements, the creep is largely controlled by the binding phase calcium-(aluminum-)silicate-hydrate, or C-(A-)S-H. This phase has a lamellar structure and under deviatoric stress aligns its *c*-axis with the principal stress. However, the limiting resistance to this reorientation is unknown at the nanocrystalline level. Small-angle X-ray scattering shows that the lamellae thickness decreases under 100's MPa deviatoric stress. Deviatoric stress Raman spectroscopy shows that there are two ways that this break-up can occur. If the material's silicate chains are cross-linked, then strain in Si—O bonds does not increase above certain stresses, indicating a relaxation adjacent to the Si—O bond. If the chains are not cross-linked, then the silicate chains are broken up by rastering against each other, introducing defects. These results show that the plastic deformation of C-(A-)S-H is relevant for Portland cement creep.

1. Introduction

The long-term deformation of concrete whereby it flows, or "creeps", under deviatoric stress is important for predicting the life expectancy of the structure and its mechanical properties. Understanding the mechanism of creep could enable designing cement chemistries that have tailored creep compliance. It is desirable to have a high creep value for mass concrete, or any concrete that develops large thermal gradients during the hydration process, because creep alleviates the thermal stress that could initiate cracks. In most structural concretes that are prestressed to strengthen against tension, creep absorbs the prestress and reduces concrete performance, and hence a small creep value is desired.

Once set, the creep response is largely controlled by the main binding phase in Portland cement, nanocrystalline calcium-(aluminum-)silicate-hydrate (Fig. 1). C-(A-)S-H has a layered structure of two-dimensional Ca seven-fold coordinated with O, OH, and H_2O sheets (the "intralayer") decorated with one-dimensional silicate chains. The uptake of aluminum ions promotes cross-linking of silicate chains on opposite sheets when synthesized above 80 °C [1,2]. Between the sheets and the silicate chains are coordinated calcium ions and strongly bound water molecules (the "interlayer"). Standard notation for silica tetrahedra is used here, with Q^1 denoting a silica tetrahedron bound only to one other tetrahedron, Q^2 a silica tetrahedron bound to two others, and Q^3 a silica tetrahedron bound to three others.

In this paper, we compare two types of C-(A-)S-H to understand how their structures affect their mechanical properties. The first type is a cross-linked structure (Fig. 1a, c), which contains aluminum. The second is a non-cross-linked sample (Fig. 1b, d), which does not. We refer to these as C-A-S-H and C-S-H, respectively. At the mesoscale, C-(A-)S-H grains have a lamellar, turbostratic morphology [3] (Fig. 1e). This has been established from Rietveld refinement [1], small-angle X-ray scattering (SAXS) [4,5], and transmission electron microscopy [6]. The short dimension of a lamella is coincident with the *c*-axis. Around each grain is a several-Å-thick layer of gel water [7,8].

Under a deviatoric stress the lamellae orient so that the *c*-axis is aligned with the principal compression direction [9], but the mechanism (s) of reorientation remains unclear. For this preferred orientation to develop, either or both of the following must be true: grains slide past each other along their *ab* faces in an intergrain mechanism ("shape preferred orientation"), or a slip plane along the *ab* plane within the crystal is activated in an intragrain mechanism [10] ("lattice preferred orientation").

* Corresponding author at: 201 Gilman Hall, University of California, Berkeley, CA 94720, United States.
E-mail address: carraro@berkeley.edu (C. Carraro).

https://doi.org/10.1016/j.cemconres.2021.106476
Received 20 November 2020; Received in revised form 26 March 2021; Accepted 30 April 2021
Available online 6 May 2021

The intergrain resistance is sometimes aided by gel water. Simulations and nanoindentation experiments have shown the lubricating effect gel water has [11–14], especially for thicker water layers, and micro/nanoindentation studies link the creep of cement paste with creep of C-S-H using a semiempirical void-filling model [12,13,15–17]. These semiempirical models are very useful for existing cements, but the models' fit parameters are not derivable from the structure of the C-S-H, e.g. why C-A-S-H has a lower creep compliance than C-S-H [16]. Grain roughness [18] could also play a role, although this parameter is difficult to measure directly. The barriers to movement at low relative humidity or low porosity remain unknown.

Intragrain resistances are plausible given that C-(A-)S-H has a similar structure to micas, a layered clay mineral, which require only 100's MPa to activate sliding on the *ab* plane [19,20]. The analogy to micas is consistent with computations showing that the lowest energy plane to expose in 11 Å tobermorite is the (004) plane [21], which coincides with the intralayer.

In this paper, we present results obtained from compacted pellets of C-S-H and C-A-S-H prepared using uniaxial stresses of 740 MPa. We track changes in their grain size with SAXS. We observe a decrease in grain thickness from ~70 Å to ~50 Å in both samples after they have been subjected to 740 MPa uniaxial compression. We do not observe any decrease in effective radius. The plastic deformation observed by SAXS signals bond-breaking events. Therefore, we probe the chemical environment of the silicate tetrahedra with Raman spectroscopy, both ex-situ and in-situ during compaction with Raman spectroscopy in a diamond anvil cell. We find that in the C-A-S-H sample under high stresses, the Raman peak corresponding to the Si–O–Ca(intralayer) stretch does not increase in vibrational energy, meaning that its bond strain does not increase, while the interlayer Si–O–Si bending peak does increase in energy. This indicates a relaxation of the intralayer in C-A-S-H. In contrast, both of these bonds develop strain in the C-S-H sample, suggesting that the slip plane in C-S-H is the water-rich interlayer, *not* the intralayer. The deviatoric stress Raman spectroscopy experiments show that the slip plane that leads to a decrease in grain thickness is different between cross-linked C-A-S-H and non-cross-linked C-S-H.

2. Methods

2.1. Samples

The C-(A-)S-H powders were synthesized by a standard method described elsewhere [9]. Briefly, samples were synthesized at 80 °C for 56 days with Ca to Si reagent ratio of 1.0, and in the case of the C-A-S-H samples, with Al/Si = 0.1. Note that while X-ray diffraction (XRD) of the C-S-H sample (Fig. S1) shows that the (002) basal peak that can be deconvoluted into two basal peaks, with thicknesses 24.4 Å and 27.6 Å, we treat this sample as homogeneous in the 24.4 Å because this spacing is five times more abundant. The basal spacing of the C-A-S-H is 11.6 Å. Samples were stored in vacuum box when not in use. Previous NMR characterizations of these samples are provided elsewhere [2], showing 17% Q^1 in the C-A-S-H and 23% Q^1 in the C-S-H, and 14% Q^3 in the C-A-S-H and 0% Q^3 in the C-S-H. The mean chain length in the C-A-S-H is 19.8 and is 8.8 in the C-S-H.

2.2. Pellet pressing

Pressed pellets of the samples were formed by loading the powder into a die and applying 740 MPa uniaxial stress in a pellet press for 60 s. Previous XRD experiments have shown that the response to such a high uniaxial stress is quite fast [9]. We define pressure and deviatoric stress as in Eqs. (1) and (2):

$$P = \frac{1}{3}*(\sigma_S + 2*\sigma_T) \quad (1)$$

$$S = \frac{1}{3}*(\sigma_S - \sigma_T) \quad (2)$$

where P is the hydrostatic pressure, σ_S is the uniaxial stress, σ_T is the average transverse stress, and S is the deviatoric stress.

The uniaxial stress of 740 MPa was chosen to enable comparison with previous high-pressure deviatoric stress XRD results [9] and the stresses accessible by the deviatoric-stress Raman spectroscopy system described below. Lower stresses have larger uncertainty because of the lower accuracy at such stresses. Higher stresses were not accessible because of the mechanical limit of the stainless steel die used.

The 740 MPa uniaxial stress (σ_S) applied to the powder to form the pellet is less than the deviatoric stress felt by the powder in the diamond anvil cell experiments. Applying an effective Poisson ratio to the powder of 0.3 [22,23] leads to a transverse stress (σ_T) equal to ~300 MPa and a deviatoric stress of 130 MPa while forming the pellet. This estimate of the deviatoric stress S is an upper bound because the effective Poisson ratio for powders is greater than the value for a solid material.

The pressed pellet method was chosen because it allows the collection of a large volume of sample to be readily analyzed by the synchrotron beamline described below. Aligning a sample that had come from a diamond anvil cell gasket is practically impossible because samples become cemented with the gasket.

2.3. Small-angle X-ray scattering

Small-angle X-ray scattering (SAXS) were carried out at beamline

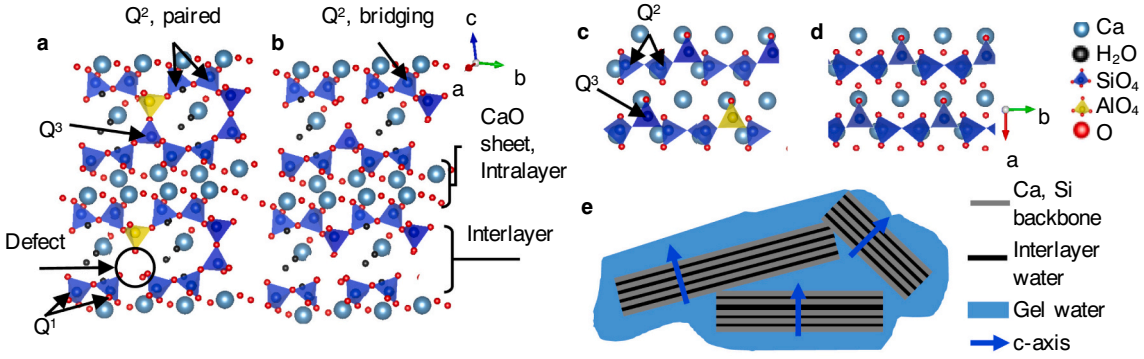

Fig. 1. Structure of the calcium-(aluminum-)silicate hydrate (C-(A-)S-H) sample in this work. (a, b) *bc* plane of C-A-S-H and C-S-H, respectively. (c, d) *ab* plane of C-A-S-H and C-S-H, respectively. Half-filled symbols denote half-occupancy in the structure. For simplicity, in the *ab* slice, only the oxygens that are involved in the Si—O symmetric stretches studied in this work are included, while water molecules, interlayer calcium ions, and the third silicon atom on the Q^3 sites are not shown. Both structures adapted from structure of cross-linked 11 Å tobermorite [5,6]. (e) Simple model of C-(A-)S-H lamellae at the mesoscale, showing the difference between strongly bound interlayer water and surface adsorbed gel water. The *c*-axis of the three grains is drawn. (not to scale).

7.3.3 at the Advanced Light Source at Lawrence Berkeley National Lab with a beam energy E = 10 keV, a bandwidth ΔE/E = 1% and a beam size about 300 × 700 μm^2 with a q-range between 0.004 and 0.4 Å^{-1}. Pressed pellets were loaded into 1 mm diameter capillaries by lightly breaking up the pellet by hand in a mortar and pestle and collecting the powder into a capillary. Scattering patterns were recorded on a two-dimensional Pilatus 2 M detector (Dectris), which has a pixel size of 172 μm. The exposure time used was less than 5 s. The X-ray beam position on the detector and the sample to detector distance were calibrated using the standard silver behenate. The two-dimensional data were calibrated and azimuthally averaged into one-dimensional intensity, I, vs. scattering vector, q, using Igor Pro Nika package [24]. The 1D data were analyzed by numerically integrating the full form factor for a disk [25], assuming a discretized normal distribution of thicknesses (i.e. contribution only from integer multiples of the basal spacing) and with a constant aspect ratio for each sample (Eqs. 3a-3e):

$$I(q) = I_0 \sum_{i=1}^{inf.} F_i^2(q)*S(q)*\text{Weight(i basal spacings)} \quad (3a)$$

$$\text{Weight(i basal spacings)} = exp\left(\frac{-(i-\mu)^2}{2\sigma^2}\right) \quad (3b)$$

$$F^2{}_i(q) = \int_0^{\pi/2} abs\left(\frac{sin(qT_i cos\phi)}{qT_i cos\phi} * \frac{2J_1(qR_i sin(\phi))}{qR_i sin(\phi)}\right)^2 sin(\phi) d\phi \quad (3c)$$

$$T_i = 0.5*i*\text{basal spacing} \quad (3d)$$

$$\text{Aspect ratio} = \frac{R_i}{T_i} = \text{constant} \quad (3e)$$

where $I(q)$ is the intensity at the scattering vector q, I_0 is an intensity factor, $S(q)$ is the static structure factor, $F_i(q)$ is the single particle form factor, i is an index for the number of basal spacings in the grain, μ is the mean number of basal spacings, σ is the standard deviation of the distribution, T_i is half the sample thickness, R_i is the average particle radius (related to the thickness by the aspect ratio), ϕ is the angle between the normal to the disk plane and the scattering vector q.

A constant aspect ratio assumption is preferred over a constant radius assumption because (i) it is more physical based on equilibrium crystal shapes, and (ii) the constant aspect ratio assumption gives a better fit. In this fit, the scale factor, the average thickness, and the sample aspect ratio are the only fit parameters. The fit thickness is nearly the same if an empirical Guinier-Porod model [4,26] is applied, although the goodness-of-fit is better using the full form factor. The full form factor also has the advantage of giving a stable fit grain radius to varied starting conditions, whereas the empirical model does not have the q-range to fit the average grain radius.

The results were highly reproducible within a single sample. Representative fits for each sample are given in Fig. S2. The error for least-squares fitting was defined as: Error(I(q)) = log(I(q), experiment) − log(I(q), fit))^2. The log(I(q)) operation is needed because of the power-law dependence of the scattering.

The fitting procedure was taken after Ref. [27], which studied sheet silicates with various intercalates. First, the patterns were fit to Eqs. (3a)-(3e) assuming S(q) = 1, i.e. assuming no interparticle orientation effects or a dilute suspension. This assumption is a useful for the first fit because form factor scattering dominates the pattern, and because as will be shown below, there are very weak oscillations or peaks from interparticle scattering that would corrupt our regression. Once the pattern has been fit, the measured intensity I(q) is divided by the fit form factor intensity F^2(q) to yield an effective S(q) [27].

2.4. Ambient Raman spectroscopy

Ambient Raman spectra were recorded by loading the powder or pellet onto a glass slide. The spectra were acquired in backscattering geometry at room temperature with a JY-Horiba Labram spectrometer with an 1800 groove/mm grating. A HeNe laser (632.8 nm) provided the excitation line through an Olympus BX41 confocal microscope, which was focused on the sample by a 50× long working distance objective (Olympus SLMPLN 50× objective, focal length = 180 mm). The spot size was less than 1 μm. Peak assignments for vibrations considered in this work are given in Table 4. Standard deviation of the measured peak centers is 0.8 cm^{-1} for the Q^2 bending peak and 1.2 cm^{-1} for the Q^2 stretching peaks in both samples. Typical standard error of the fit peak center is 1 cm^{-1}. Incorporation of Al in C-A-S-H does not lead to meaningful increases in peak width compared to the C-S-H sample [28,29].

2.5. High-pressure and deviatoric stress Raman spectroscopy

The experiments described below were performed on the same Raman spectrometer described in Section 2.4. Hydrostatic high-pressure Raman spectra were acquired by loading the sample into a BX90 diamond anvil cell by a standard procedure with a pressure medium, either a 4:1 volume/volume mixture of methanol to ethanol, or silicone oil [34]. It was necessary to use multiple pressure media so that the sample peaks could be observed without interference from the pressure media peaks [29]. Methanol-ethanol mixtures have interfering peaks around 1000 cm^{-1}, while silicone oil has an interfering peak around 650–700 cm^{-1}. Typical exposure times were 20 min with a 10 mW laser. The power of the laser is defined at the source. The standard ruby lines could not be used for hydrostatic pressure measurement when measuring the minerals in this study because the high laser power needed for the calcium silicate hydrate samples activates the ruby fluorescence, resulting in unacceptable convolution with the samples' weak Raman lines. Instead, the pressure in the diamond anvil cell was obtained from the Raman frequency of the top diamond culet, as described elsewhere [29].

Deviatoric stress Raman spectra were acquired by lightly packing the powder into a BX90 diamond anvil cell in a stainless steel gasket, with multiple well-spaced ruby spheres loaded onto the top diamond before assembling the diamond anvil cell (Fig. 2). We were able to record the spectra of C-(A-)S-H in the diamond anvil cell under deviatoric stress despite rubies in the sample chamber because the compaction of the sample by the deviatoric stress increases the packing density of the C-(A-)S-H powder and therefore the signal is strong enough to be seen. A spot in the gasket was consistently sampled throughout the deviatoric stress experiments. C-(A-)S-H Raman spectra were deconvoluted with CasaXPS software using mixed Gaussian-Lorentzian functions. Typical standard error from the regression of the peak center is 2.0 cm^{-1} for both peaks for spectra recorded in a diamond anvil cell.

Although peak widths increase by ~30% in the diamond anvil cell when the material is under pressure and the grains may deform their shape, the regression uncertainty for the peak center remains roughly 2.0 cm^{-1} for the pressure range studied here in hydrostatic and deviatoric conditions.

When combining the separately obtained Q^2 bending and stretching peaks, as in the hydrostatic points of Fig. 5, a linear relationship between wavenumber and pressure was assumed for one mode – in the C-S-H sample, the Q^2 bending peak, and in the C-A-S-H sample, the Q^2 symmetric stretch peak [29]. The frequency of that mode was estimated at the pressure of the other mode.

The error bars for the hydrostatic points in Fig. 5 are either the

Table 4
Peak assignments for Raman spectroscopy of calcium-aluminum-silicate hydrates relevant to this work.

Ambient position (cm^{-1})	Assignment [28,30–33]
675	Si-O-Si Q^2 bending
850	Si-O-X Q^1 symmetric stretch
1010	Si-O-X[a] Q^2 symmetric stretch
1075	$CaCO_3$

[a] X ≠ Si, Al.

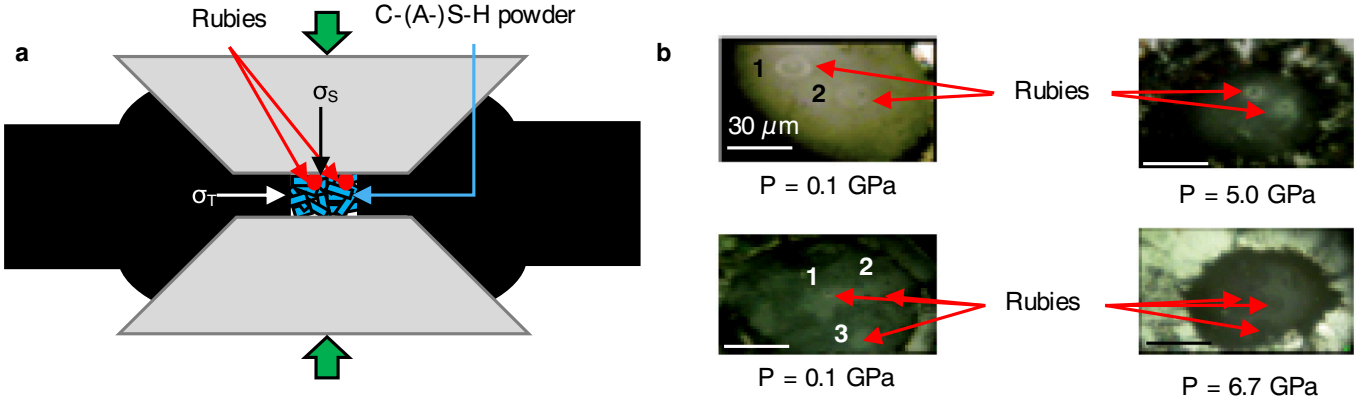

Fig. 2. (a) Cartoon of set-up, showing top and bottom diamond (gray), stainless steel gasket (black), and stress field. (b) Optical images of gasket at beginning of experiment and at 5.0 GPa hydrostatic pressure. Images enhanced to improve rubies' contrast. Top images: C-A-S-H sample. Bottom images: C-S-H sample. Scale bar 30 μm for all.

contributions from the spectrometer imprecision, repeatability uncertainty, and peak fit center standard error; or two standard errors of the regression line between the Q^2 bending peak with pressure in C-S-H (two standard errors = 3.00 cm^{-1}) or between the Q^2 symmetric stretching peak in C-A-S-H with pressure (two standard errors = 5.81 cm^{-1}). Different modes were used as the basis for the plot because the linearity between peak center and pressure was better for different modes between the two samples. These plots are available from our previous work [29].

Calcium oxide vibrations at low wavenumbers were not resolvable in the diamond anvil cell, neither were Q^3 bending vibrations seen in tobermorites [30] (Fig. S8, S9). Q^3 vibrations are not intense enough to observe by Raman spectroscopy even though these tetrahedra are present in the C-A-S-H sample [2,29].

2.6. Determining stress field in deviatoric stress Raman spectroscopy

Components of hydrostatic pressure *P* and deviatoric stress *S* were determined by the shift in the ruby R_2 line and by the difference between the R_1 and R_2 lines, respectively [35] (Fig. S3). The ruby R_2 wavelength depends only on pressure within the deviatoric stress range in this study [35]. Ruby R_1, R_2 peak positions were determined by deconvolution with CasaXPS software using pure Lorentzian functions. The equations used to calculate P and S as functions of the R_1 and R_2 wavelengths are given in the SI, Eqs. ES1-ES2.

Deviatoric stress naturally arises in powder samples in the diamond anvil cell with the stress along the direction normal to the diamonds being greater than the transverse stress imposed by the gasket. Although we cannot control the initial orientation of the ruby spheres, we observe that all five rubies show an increase in the wavelength difference between the two peaks once deviatoric stress is applied (Fig. S4), leading us to conclude that the rubies are oriented with their *a*-axis nearly along the direction of the stress [35]. The magnitude of the reported stress should therefore be considered an upper bound of the stress felt by the ruby. We define pressure and deviatoric stress as in Eqs. (1) and (2).

The uniaxial stress is the stress along the axis of the diamonds. We calculate these properties in the rubies [35], take the average result, and assume this stress field being felt by the powder. This "equal-stress" assumption for every grain in the diamond anvil cell (also known as the Reuss approximation) is standard in geophysics and materials research using diamond anvil cells under deviatoric stress [9,36,37].

2.7. Theory of deviatoric-stress Raman spectroscopy applied to C-(A-)S-H

Raman spectroscopy in a diamond anvil cell is used to study chemical bond strain while deviatoric stress is applied. To understand how to interpret deviatoric-stress Raman spectra, it is necessary to start from hydrostatic Raman spectroscopy.

The key concept of hydrostatic Raman spectroscopy is that chemical bonds have characteristic anharmonicity γ_i, also known at the mode Grüneisen parameter, which is the relative change in the relative vibrational frequency with the strain of the vibration [38], in Eq. 4:

$$\gamma_i = -\frac{dlog(\omega_i/\omega_0)}{dlog(V_i/V_0)} \quad (4)$$

where *i* is an index indicating the calculation is for a particular bond, 0 is an index indicating the ambient value, ω is the frequency of the chemical bond vibration and *V* is the average volume of the chemical bond that changes with pressure. The value of the anharmonicity is not necessarily the same over a large strain range, but vibrational mode frequency and vibrational mode volume are always linked.

The mode Grüneisen parameter can be measured when high-pressure X-ray diffraction data are combined with separately obtained high-pressure Raman data. In simple structures with only one or two characteristic interatomic distances, the volume change of the bond with pressure can be rigorously (and trivially) assigned to the volume change of the unit cell. In more complex unit cells, the volume change is rigorously assigned to the *volume of the oscillation* that changes under compression [38]. We have previously discussed how this analysis can be used to learn about bond characteristics in C-(A-)S-H towards improved force fields and designing new cements [29]. In this work we invert the relation in Eq. (4) to note that the frequency has a characteristic relationship to volume strain.

The Q^2 symmetric stretch at ω_0 ~1000 cm^{-1} is in a plane nearly perpendicular to the b-axis and with the CaO intralayer. We will call the intralayer *c_intralayer*. The distinction between the entire axis *c* and the *c_intralayer* is necessary because the compressibilities are so different [34]. The intralayer volume change is proportional to the area of the *a-c_intralayer* plane to a good approximation. The Q^2 bending at ω_0 ~ 670 cm^{-1} is bending between the *b*-axis and *c*-axis, so its volume change is proportional to the area of the *bc* plane. Garbev et al. noted that Q^2 bending frequency increased as the paired angle decreased [32] in crystalline calcium silicate phases. Our earlier work with hydrostatic Raman spectra in C-S-H [29] showed this frequency monotonically increasing, which suggests that the bond angle should be decreasing, as some calculations of C-S-H phases suggest [34]. However, correlations that are observed between crystalline phases will not necessarily hold within a phase as it is compacted.

The error bars in the strain for the hydrostatic points were determined by using two standard errors of the pressure uncertainty (~0.16 GPa [29]) and applying this to the compliance tensor, always assuming a hydrostatic condition. The error bars of the strain for the deviatoric

points were determined with two sample standard deviations of the stress field. For more details, see the supplementary material, Eqs. ES3-ES10. The assumptions we have applied have led to the widest reasonable error bars.

The compliance tensor is applied assuming that all *c*-axes are oriented perfectly towards the diamond axis – and given that nearly all of the grains are oriented within 20° of the deviatoric stress vector at ~800 MPa uniaxial stress [9], this assumption is reasonable. The assumption means that *c*-strains are overestimated in the deviatoric case, especially for the first few data points when grains have not yet ordered, because the *c*-axis strain is the most sensitive to orientation in the stress field. This has only a small effect on the C-A-S-H sample, because its compliance tensor is fairly isotropic. In the C-S-H sample the orientation assumption probably overestimates the strain in the *c*-axis, because the *c*-axis is the softest axis in the material.

The deviation between *mode strain* and *unit cell strain* has to be observed by comparing the vibrational frequency at a particular unit cell strain for two conditions. The first condition is hydrostatic, with only elastic deformation (in our case, in pressures of at least 10 GPa in a pressure medium). This assertion is made by observation that the diffraction pattern of the samples is nearly identical after unloading the sample from a DAC during a high-pressure XRD experiment [1]. The second condition is a deviatoric stress high enough to cause plastic deformation.

To summarize: vibrational mode strain is linked to vibrational mode frequency. If the mode strain is evolving differently under conditions known to cause plastic deformation (i.e., deviatoric stress) vs. conditions where there is no plastic deformation (i.e., hydrostatic), *after accounting for the unit cell strain*, then that mode is identified as being linked to the plastic deformation.

2.8. Deviatoric stress Raman spectroscopy: Stress field in diamond anvil cells

In this experiment, powders are loaded into a gasket with several rubies as stress field gauges and the powders' Raman spectra are measured at each tightening position. The pressure and deviatoric stress felt by each ruby at each measurement point and the average condition applied to the powders are given in Fig. 3a–f for both samples. The agreement is quite reasonable for diamond anvil cell work, with a standard deviation of 0.4 GPa for pressure and 0.5 GPa for deviatoric stress between rubies at a particular measurement for both experiments. The magnitude of the deviatoric stress agrees well with the results of Geng et al., where a similar loading setup was used for high-pressure X-ray diffraction experiments [9].

All five ruby spheres' R_1 and R_2 lines separated at high stresses, indicating that their *a*-axes are aligned with the principal stress. The *a*-axis is softer in ruby for pressures less than 6 GPa [39], and samples tend to align their softest axis with the principal axis of stress.

Some of the rubies' lines actually decreased the separation at early stages of compaction (Fig. S4), which manifests as a negative calculated deviatoric stress component, e.g. Ruby 1, Fig. 3b, and Ruby 3, Fig. 3e. This indicates that at early stages this ruby's *a*-axis was not aligned with the principal axis of stress, but as the powder tugged at the ruby during compaction, the softest axis of the ruby (the a-axis) was pulled into alignment with the principal axis of stress.

2.9. Determining unit cell strain in samples under non-uniform stress field

The generalized Hooke's Law was used to estimate the relative change in the cell axis length. The compliance tensors were calculated with CSH-FF and taken from Ref. [9]. The tensor developed for C-A-S-H sample compares well with actual mechanical properties of the sample. The tensor developed for C-S-H in Ref. [2] compares well with the

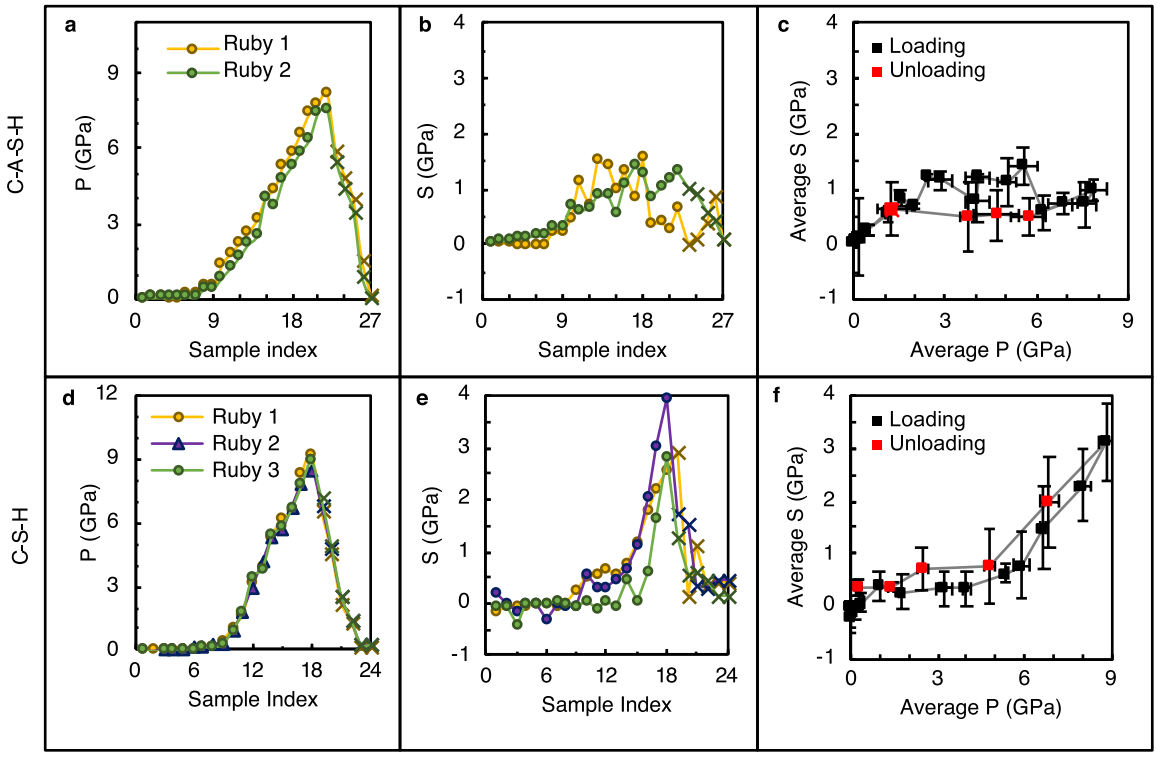

Fig. 3. Stress field in the diamond anvil cell as determined by rubies. Unless otherwise noted, cross marks indicate unloading. (a) Pressure in gasket for C-A-S-H experiment. (b) Deviatoric stress in gasket for C-A-S-H experiment. (c) Comparison of stress and pressure throughout experiment, error bars are one standard deviation of standard values. (d) Pressure in gasket for C-S-H experiment. (e) Deviatoric stress in gasket for C-S-H experiment. (f) Comparison of stress and pressure throughout C-S-H experiment, error bars are one standard deviation of measured values.

dominant phase in the C-S-H samples (sample number Al0_C1 in Ref. [1]). The generalized Hooke's law is given in Eq. 5:

$$\text{Strain}_{kl} = C^{-1}_{ijkl} * \text{Stress}_{ij} \quad (5)$$

where *kl* is a crystal or sample axis (i.e., 11, 12, …), C_{ijkl} is the full (36-component) compliance tensor, and *ij* is a stress direction *from the reference of the sample*. In the hydrostatic case, the stress is uniform everywhere and there is no bulk shear stress, so the point of reference does not affect the analysis.

In the deviatoric case the stress is not uniform everywhere, so reconciliation of the stress axes and the sample axes is not guaranteed. However, these samples show very large preferred orientation under deviatoric stress, with a large fraction of the crystals aligning their 33 or *c* axis towards the largest component of the stress field [9].

3. Results and discussion

3.1. Small-angle X-ray scattering of pressed pellets

To investigate the effect of deviatoric stress on grain size, we compacted C-(A-)S-H powders with a uniaxial stress of 740 MPa in a die in a pellet press and compared the small-angle X-ray scattering (SAXS) patterns before and after. Representative sample patterns I(q) after subtracting capillary background are given in Fig. S2, and normalized patterns are given in Figs. 4a, b. (See Methods section for further details.) The average thickness of the grains and the range of thicknesses in each case are given in Table 1. We do not find any difference between the C-A-S-H and C-S-H powder lamellae thicknesses. Differences in radii between the powders are not statistically significant.

The fit parameters in Table 1 from SAXS compare well with the parameters obtained by Geng et al. [1] as a byproduct of their Rietveld refinement, which provides an estimate of the size of the coherent scattering domain along an X-ray scattering vector. The thickness of the C-A-S-H sample by SAXS is nearly identical to the value obtained with Rietveld refinement (69.1 Å here vs 75 Å by Geng); however, the C-S-H sample appears much thicker here than by Rietveld refinement (73.4 Å vs. 35 Å by Geng). The difference arises because XRD peak widths used for Rietveld refinement are related to the mean coherent scattering length, whereas SAXS is agnostic to the crystallinity of the sample. The C-S-H sample has more defect sites (as Q^1) than the C-A-S-H sample so this is the most likely explanation for the large difference with XRD analysis in the C-S-H samples.

Fig. 4a, b normalize the intensity with a factor of q^4. This normalization is used to make changes in grain thickness more apparent for visual inspection. In a Guinier-Porod model [26], the thickness of a disk is essentially determined the scattering vector where the intensity switches from being proportional to q^4 to q^2. The further to the right this bend is, the thinner the disks. Fig. 4a, b show that this bend is further to the right in the pellet samples, indicating that the lamellae are broken up by the compaction process.

Table 1
Fit parameters in small angle scattering. Values in parentheses are one standard error, including the standard error of fit values and standard deviation of measured values. The definitions of μ, σ, and aspect ratio are given in Eqs. 3a-3e.

Sample		Average thickness, 2 * T (Å)	Standard deviation, σ (Å)	2 * Average Radius (Å)	Aspect ratio, R/T (–)
C-A-S-H	Powder	69.1 (3.5)	16.5 (1.0)	1060 (151)	0.065 (0.006)
	Pellet, 740 MPa	47.5 (4.2)	10.8 (1.6)	931 (82)	0.051 (0.000)
C-S-H	Powder	73.4 (1.0)	17.9 (0.3)	1165 (16)	0.063 (0.000)
	Pellet, 740 MPa	47.8 (1.4)	10.9 (0.4)	870 (57)	0.055 (0.002)

Grain-grain correlations in sheet silicates manifest as ripples in a plot of intensity divided by the fit form factor, $I(q)/F^2(q)$, which is effectively a fit S(q) [27] (Fig. 4c, d). In general, S(q) oscillates about 1.0 for all samples, meaning that interparticle distances and orientation effects are simply too varied to generate characteristic ripples. However, there are a few exceptions to this. First, there appears to be a peak in the pellets (red traces) at $q \sim 0.06$ Å^{-1}(red dashed line in Figs. 4c, d). Inspecting the fits, it is clear that this peak just an artifact of the fit, where the fit profile expects peaks where there are none (Fig. S2).

The second notable feature is the doublet at $q \sim 0.09$ Å^{-1} in the powder samples (black dashed line in Fig. 4c, d). This feature is present in the measured I(q), and is present at the same scattering vector for both samples (Fig. S5), and is not present after compaction. This peak likely corresponds to some local minima for opposing charged particles separated by either air or gel water, and has been observed experimentally for sheet silicates in various solvents [27]. The scattering vector magnitude corresponds to a particle–to–particle distance of 70 Å, which is roughly the size of the particles. This intensity is not observed in an empty capillary's pattern (Fig. S6). Local minima for interparticle spacing on the order of 10's – 100's Å are common in colloidal systems, and to our knowledge this is the first direct experimental evidence of such a stable spacing for C-S-H in the powder phase, vindicating several calculations predicting a similar value [40,41]. The similarity in value of the magnitude of the scattering vector for both samples is a result of their homologous structures; both are expected to expose the intralayer (004) plane [21,42]. The third notable feature is the broad peak in I(q)/

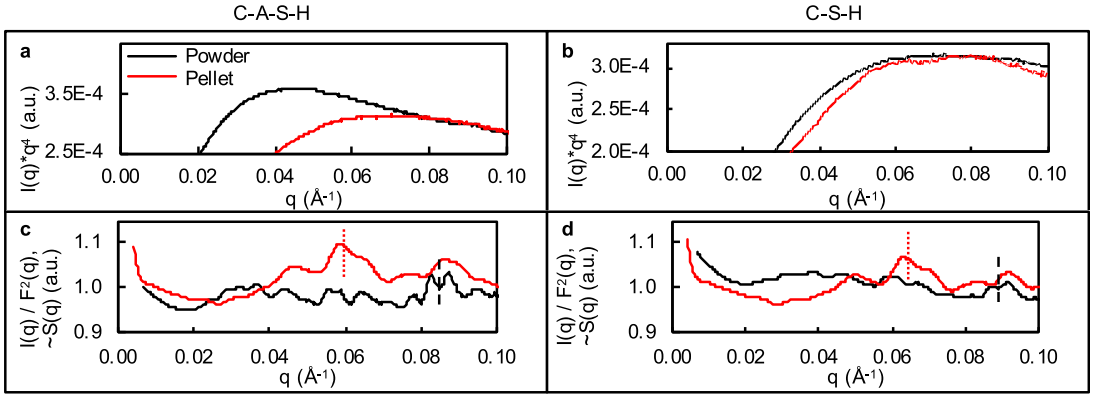

Fig. 4. SAXS of C-A-S-H and C-S-H powders subjected to loading conditions. Patterns have had capillary background subtracted and been rescaled. (a, b) q^4-normalized scattering intensity of powder and crushed pellet for easier inspection to determine grain thickness in C-A-S-H and C-S-H, respectively. (c, d) Effective interparticle structure factor S(q) for powder and crushed pellet. Red dashed lines mark an artifact of the fit; black dashed lines mark intergrain spacing. (For interpretation of the references to colour in this figure legend, the reader is referred to the web version of this article.)

$F^2(q)$ around q ~ 0.04 $Å^{-1}$. This is a grain-grain correlation, as it is present at roughly $q = 2\pi/2$ T [43], and corresponds to grains stacked on top of one another.

Compaction generally leads to more long range order [44], which should manifest as intense ripples in a SAXS pattern, yet the SAXS pattern of the compacted pellets shows no ripples, and the only "peaks" in the effective S(q) are annihilated by the compaction. This paradox is resolved by the inhomogeneity of lamellae dimensions and the spacings between lamellae in the compacted powders. The compaction at 740 MPa imparts enough stress on the lamellae to break them apart and disrupts the stable 70 Å spacing structure from the powder. The heterogeneity of the compaction prevents intensity from building up at any characteristic *q* [43]. Further experiments based on X-ray diffraction patterns of compacted C-S-H may yield more detailed insights to the compaction mechanism.

SAXS pattern of the samples show a decreased thickness in pressed pellets, but it is unknown how this occurred at a chemical-bond level. To answer this question, we used Raman spectroscopy to track bond strain and the relative population of silica tetrahedra of C-(A-)S-H powders under deviatoric stress.

3.2. High-pressure hydrostatic and deviatoric Raman spectroscopy

The evolution of the silicate mode frequencies with pressure was measured using Raman spectroscopy. The mode frequency is closely tied to the mode strain. As the volume of the mode decreases with compaction, the frequency and the associated Raman shift increase. Applying the stress field from the rubies to the compliance tensor of the material shows that once the powders are compacted in the cell (i.e. after sample index 9 in Fig. 3) all of the crystal axes decrease in length.

Fig. 5 displays the silicate mode frequencies under deviatoric stress and hydrostatic stress, conditions that lead to plastic and elastic strain, respectively. (For mode frequencies versus pressure, see Fig. S7a-d; for mode frequencies versus estimated unit cell strain, see Fig. S7e-h). Pressure coefficients are given in Table 2. Representative raw data for the hydrostatic and deviatoric loads can be found on Figs. S8, S9. Further discussion of hydrostatic pressure Raman spectra is given in Ref. [29]. Strikingly, in the C-A-S-H sample, the Q^2 Si–O symmetric stretch strain diverges from the Q^2 Si–O–Si bending strain in the deviatoric condition, while the C-S-H sample shows essentially the same relative increase in mode strains for both conditions. The divergence in the diamond anvil cell is resolvable when the stresses are at least P ~ 4 GPa, S ~ 0.7 GPa (although plastic strains are known to occur at lower stresses by the SAXS experiments).

One explanation for the divergence is the difference in stress field between the two cases; in the deviatoric case, the c-axis takes more of the total strain, so the bending mode associated with the c-axis should be relatively more strained in the deviatoric case. However, even after accounting for the relative strain in the unit cell axes, the C-A-S-H vibrational modes still diverge (Fig. S7e, g). In fact, after accounting for the relative unit cell strains, the C-S-H vibrational modes evolve in the same way for both hydrostatic and deviatoric conditions (Fig. S7f, h).

Table 2
Vibrational Si-O-Si properties of samples studied in this work.

Sample	Mode	Ambient frequency (cm^{-1})	dω/dP, Hydrostatic (cm^{-1}/GPa)	dω/dP, Deviatoric (cm^{-1}/GPa)
C-A-S-H	Q^2 bending	675	2.4	3.6
	Q^2 symmetric stretch	1010	6.5	4.2
C-S-H	Q^2 bending	669	3.1	4.5
	Q^2 symmetric stretch	1012	5.5	5.5

The large divergence in Q^2 symmetric stretch bond strain in C-A-S-H under deviatoric stress indicates a relaxation near the Si–O (–Ca) bond. This mode frequency is a qualitative descriptor of the Si – O bond strain. The bond does not develop more strain under the deviatoric stress even as the other modes do; an upper bound for the minimum deviatoric stress to achieve this relaxation is 740 MPa applied to a powder by comparison with the SAXS results above. The resolution of the high-pressure Raman experiment is not sufficient to detect the relaxation at such low stresses, but at higher stresses the relaxation is apparent.

We assign the deformation to a slip plane adjacent to the Si – O bonds in C-A-S-H. The intralayer is the most reasonable motif to slip. This hypothesis is in good agreement with the comparison to micas and with the surface energy discussion in the Introduction. Breakage of the Q^3 and Q^2 silica tetrahedra is not favored over the CaO interlayer because Si – O bonds have a valence unit near 4/4, whereas Ca–O bonds are more like 2/7 or 2/8 [45].

The explanation of the bond strain evolution with stress is represented by Fig. 6, which is inspired by (i) models of plastic deformation in clays that suppose sheets shear against each other [46] and (ii) a nanomechanical origin of structural strength [47]. At ambient conditions, the powder is isotropic and the unit cell has no deformation (Fig. 6a, b). At low compressive stresses the lamellae start to compact and shear against each other [48] (Fig. 6c, d). Eventually the stresses cause the lamellae to be sheared apart (Fig. 4e, f). Bond strains are qualitatively plotted in Fig. 4g for various constituent chemical bonds. From right to left: the O–Ca bonds are softer than Si–O bonds, and suffer greater strains until they slip. The oxygen member of the O–Ca bond is also bonded to a silicon atom, which means that after the slip, the Si–O bond strain does not increase its strain as much (Fig. 6g). The Q^2 bending is unaffected by the slip because it is not party to the bond breaking

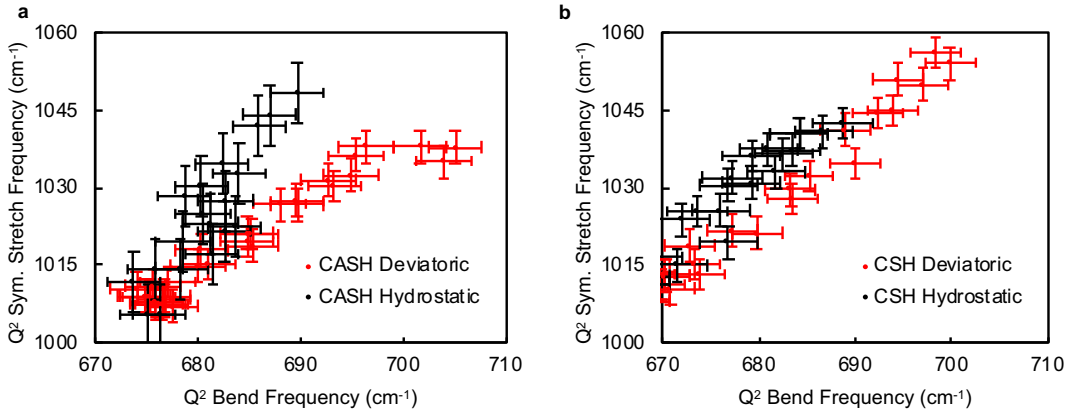

Fig. 5. Evolution of Raman shift of selected Si-O-Si modes in hydrostatic and deviatoric conditions. (a) In cross-linked C-A-S-H, (b) in non-cross-linked C-S-H. In hydrostatic compression, deformations are mostly elastic; in deviatoric compression, plastic deformations are observed.

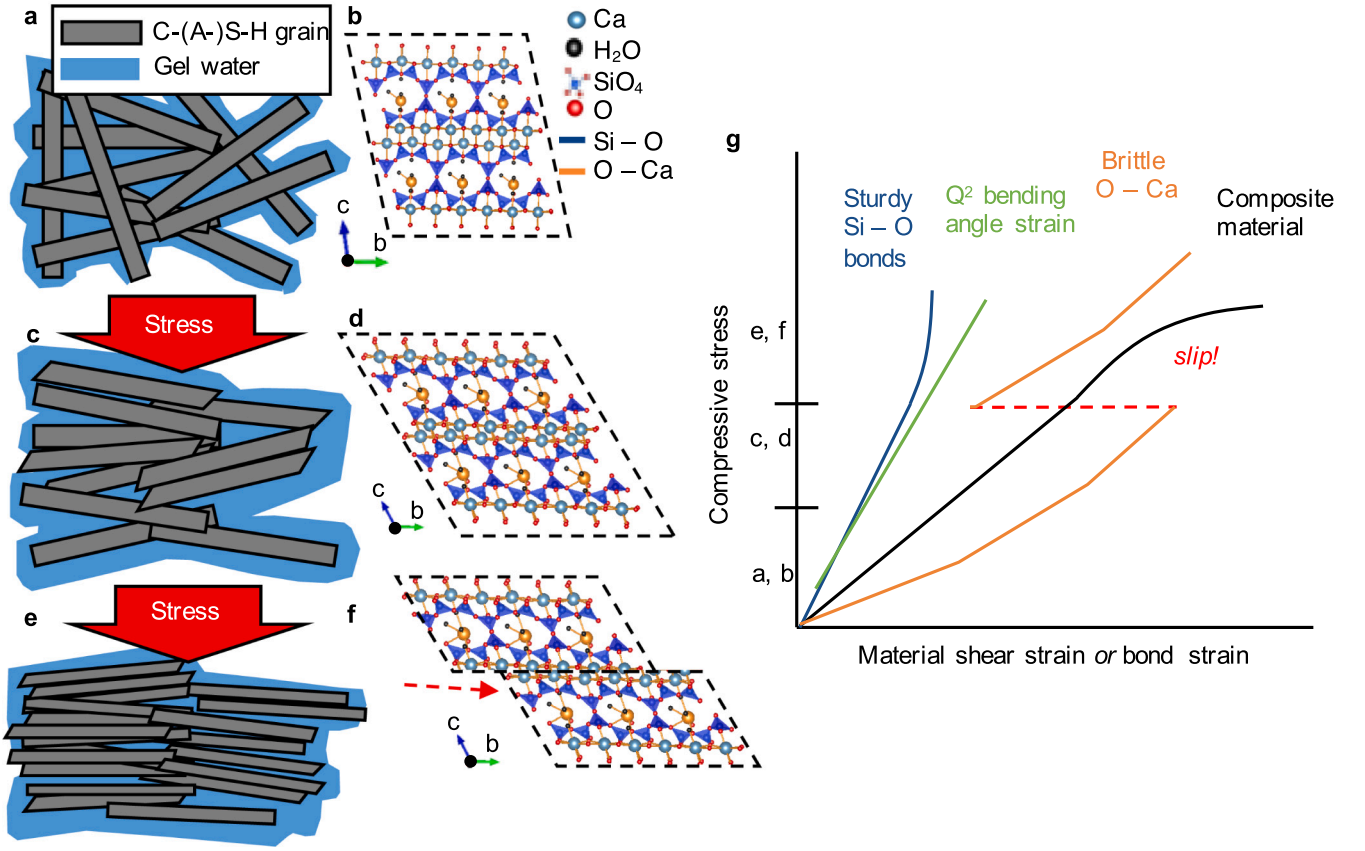

Fig. 6. The link between plastic deformations and chemical bonds in C-(A-)S-H. (a) Powder at ambient pressure. (b) Schematic of C-(A-)S-H at ambient pressure. (c) Powder under small deviatoric stress is elastically deformed (d) Unit cell at stress below the material's elastic limit. (e) Powder under large deviatoric stress is plastically deformed, lamellae are broken apart, and preferred orientation develops. (f) Unit cell at stress above the elastic limit, here slipping on the intralayer. (g) Qualitative stress-strain plot of the material and its chemical bonds. Stress axis ticks correspond to the noted part of this figure. The figure is inspired by models of clay compaction [46] and the nanomechanical origins of structural strength [47].

event.

We do not observe any evidence of a deformation or relaxation around the silica tetrahedra modes in the C-S-H sample, so the mechanism that achieved decreased grain thickness must be by a separate mechanism. If the environment around the Si-O-Ca(intralayer) bonds remains nearly isomorphic, as suggested by Fig. 5b, then the plane that slips must be the interlayer. Sliding along the interlayer would result in bridging tetrahedra rastering against each other, which would decrease the extent of polymerization and increase the number of Q^1 sites in the structure. Recent characterization of a similar C-S-H sample using X-ray Raman spectroscopy under deviatoric condition with P ~ 20 GPa showed a permanent deformation in Ca–O bond length, which was assigned to deformation in both the interlayer and the intralayer [49].

The Q^1 stretching region in C-S-H grows relative to the Q^2 stretching region (Table 3, Fig. S10). This peak is chosen for normalization because its intensity shows the least dependence on the sample orientation effects [29]. We also examined the compacts by Raman spectroscopy at ambient conditions and at stresses ranging from 240 to 740 MPa, which show the same trend as the powders in the diamond anvil cells. (Fig. S11).

Table 3
Relative height of Q^1 peak compared to Q^2 bending peak of powders in diamond anvil cell.

Condition	C-A-S-H	C-S-H
Ambient	0.05	0.06
S ≈ 0.5 GPa	0.06	0.16
Unload	0.05	0.16

The height ratio is used for comparison because it is more stable compared to the area ratio (the width of the Q^1 peak is highly dependent on the area selected for fitting). Curiously, in the diamond anvil cell and the pellet pressing experiments, the C-S-H Q^1 area increases at low stresses but does not increase at greater applied stresses (Fig. S7b, S8b). One possible explanation is that the Q^1 may "scavenge" each other during slip, so that as more are generated by the deviatoric stress, they react with each other when encountered to form Q^2 in stress-induced polymerization. Silicate polymerization is known to occur when C-(A-)S-H grains are carbonated in air [28].

The final evidence of plastic deformation in the samples is the growth of the calcium carbonate peak beyond what would be expected from a sample in air (Fig. 7). In both samples the calcium carbonate peak grows relative to the Q^2 peaks. Calcium carbonate grows from accessible calcium atoms and carbon dioxide. Plastic deformation, especially sliding along (004) intralayer, would expose more calcium atoms to carbon dioxide in the air. Over the course of the experiment (three days), the height ratio of $CaCO_3$ to Q^2 symmetric stretch grows from 0.7 to 1.4 for both samples. In the same powder allowed to react with carbon dioxide in air over ten days, the ratio only reaches ~1. The excess growth of carbonate phases means that calcium is made more accessible by the deformation in the DAC.

3.3. Comparison between SAXS, deviatoric-stress XRD, nanoindentation, and creep

We do not observe an increase in the Si–O bond strain in C-A-S-H by deviatoric stress Raman spectroscopy (S > 1000 MPa) until much higher deviatoric stress than the compaction experiment (S ~ 130 MPa). This

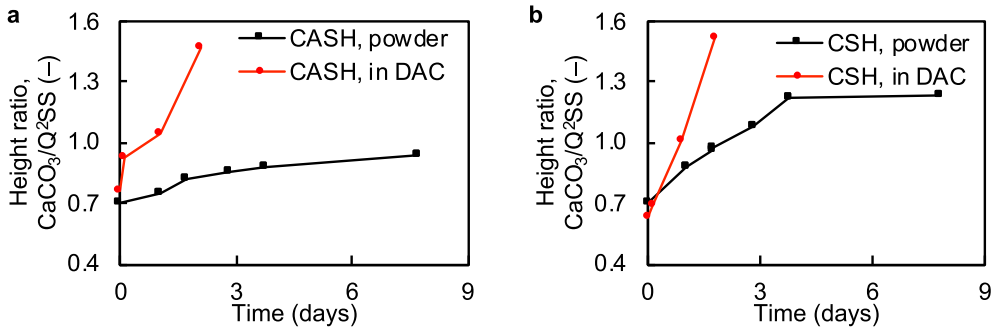

Fig. 7. Height ratio of carbonate peak to Q^2 symmetric stretch in (a) C-A-S-H, (b) C-S-H while in the DAC and while in ambient atmosphere. Points are averaged for each day. In the C-A-S-H experiment, uniaxial stress increases to 2.9, 7.5, and 10.0 GPa with each day; in the C-S-H experiment, uniaxial stress increases to 0.3, 3.6, and 9.2 GPa with each day.

may be because the effect is too subtle to be resolved at lower stresses. We postulate that the C-A-S-H must have a greater resistance to plastic deformation than C-S-H, because if the intralayer was more susceptible than the C-S-H interlayer, then both samples would show minimal Si–O bond strain at high stresses. This is not the case, so the limiting resistance must be higher in C-A-S-H.

The different mechanisms and active stress regimes we propose are in agreement with creep tests of cross-linked C-A-S-H showing much less creep than C-S-H [16]. The experiments of Ref. [16] compacted non-crosslinked C-S-H and cross-linked C-A-S-H powders into disks using ~500 MPa uniaxial stress and performed nanoindenation with an average stress of at least 10's of GPa. Other C-S-H nanoindentation experiments on the same order of stress come close to reproducing the creep behavior of macroscopic concrete [15,17,50]. Because our SAXS and Raman spectroscopy results are obtained at lower stresses than nanoindentation experiments, and nanoindentation experiments reproduce creep behavior of cements, the plastic deformation mechanisms we observe are likely relevant to extant Portland cements. When an interlayer comprises only water molecules and ions, this is the plane that slips; when the interlayer is bridged by Q^3 tetrahedra, the intralayer slips.

This phenomenon is important when the packing density is so high that intergrain sliding on gel water is not contributing. Inspecting Fig. 17 of Ref. [12], a paper that shows the effect of water molecules on the creep of cement using nanoindentation, the condition of high packing density looks to be met for an average water thickness layer of ~5 Å or less, because this is the point at which the effect of fewer water molecules does not seem to correlate with creep compliance. Incidentally this is the same thickness of water in the interlayer of 14 Å tobermorite, a non-cross-linked crystalline analog for C-S-H.

In practical terms, using the data from Ref. [12], this condition can be met at relative humidity as high as 30%, comparing Ref. [12]'s Figs. 9 and 16. In the limit of this model, this means that the creep resistance of cement matrix containing C-(A-)S-H has an upper bound in the durability of the calcium oxide intralayer sheet. Inspecting the scatter that Ref. [12] produces between its samples shows that there is still much room for tuning the creep of cements based on the phases that are formed by the mix.

More work is still needed to delineate between intragrain slip mechanisms and intergrain sliding, especially with high-pressure X-ray diffraction, to rigorously test whether the mechanisms proposed here are reproduced in real concrete specimens, and the role of other properties of C-(A-)S-H, such as grain size and shape which are known to be important for compaction dynamics [18].

4. Conclusions

Small angle X-ray scattering of C-A-S-H and C-S-H pellets pressed to 740 MPa shows a decrease in grain thickness from ~70 Å to ~50 Å, while effective grain radii are unchanged in compression. To understand the deformation mechanisms, we used deviatoric-stress Raman spectroscopy of a powder in a diamond anvil cell. This technique shows that in cross-linked C-A-S-H, Si–O bond strain does not increase much at high stresses, indicating a relaxation around Si–O tetrahedra, most likely of the seven-fold-coordinate Ca intralayer. In non-crosslinked C-S-H, bond strains evolve as expected for an isomorphic contraction. Furthermore, this sample shows a relative increase in the area of the Q^1 peak which is attributed to interlayer sliding breaking chains apart.

This work notes the decrease in average grain thickness of C-A-S-H under 130 MPa deviatoric stress and uses Raman spectroscopy to identify at a chemical-bond-level how the grains plastically deform. The results agree with nanoindentation experiments of similar materials, and the confluence of these results points to intragrain deformation being the dominant mechanism for creep in the cement matrix when the grain edges have less than 5 Å water; this condition is effectively met when the relative humidity is less than 30%. Models of creep and compaction of C-A-S-H must account for this as researchers explore new cement chemistries. More work is needed to understand if the slip planes implicated in this work dominate at all deviatoric stress regimes and what the role of grain size and shape is.

Author contributions

David W. Gardner: Conceptualization, Funding acquisition, Methodology, Formal analysis, Investigation, Writing – Original Draft, Writing – Review and Editing, Software, Validation.

Jiaqi Li: Methodology, resources, formal analysis, Writing – Review and Editing, Validation.

Martin Kunz: Supervision, Methodology, Resources.

Chenhui Zhu: Software, Resources.

Paulo Monteiro: Funding acquisition, Writing – Review and Editing,

Roya Maboudian: Funding acquisition, Project administration, Writing – Review and Editing, Supervision.

Carlo Carraro: Project administration, Writing – Review and Editing, Supervision

Declaration of competing interest

The authors declare that they have no known competing financial interests or personal relationships that could have appeared to influence the work reported in this paper.

Acknowledgements

The support of the National Science Foundation under the Division of Materials Research Ceramics Program, DMR-CER, Grant No. 1935604 is gratefully acknowledged. The authors thank Barbara Lothenbach for providing the samples synthesized by Rupert J. Myers at EMPA.

This material is also based upon work partially supported by the U.S. Department of Energy, Office of Science, Office of Workforce Development for Teachers and Scientists, Office of Science Graduate Student Research (SCGSR) program. The SCGSR program is administered by the Oak Ridge Institute for Science and Education (ORISE) for the DOE. ORISE is managed by ORAU under contract number DE-SC0014664. All opinions expressed in this paper are the author's and do not necessarily reflect the policies and views of DOE, ORAU, or ORISE.

The Advanced Light Source is supported by the Director, Office of Science, Office of Basic Energy Sciences, of the U.S. Department of Energy under Contract No. DE-AC02-05CH11231. Beamline 12.2.2 and sample preparation of this research are partially supported by COMPRES, the Consortium for Materials Properties Research in Earth Sciences under NSF Cooperative Agreement EAR 1606856.

Appendix A. Supplementary data

Supplementary data to this article can be found online at https://doi.org/10.1016/j.cemconres.2021.106476.

References

[1] G. Geng, R.J. Myers, J. Li, R. Maboudian, C. Carraro, D.A. Shapiro, P.J. M. Monteiro, Aluminum-induced dreierketten chain cross-links increase the mechanical properties of nanocrystalline calcium aluminosilicate hydrate, Sci. Rep. 7 (2017) 44032, https://doi.org/10.1038/srep44032.

[2] R.J. Myers, E. L'Hôpital, J.L. Provis, B. Lothenbach, Effect of temperature and aluminium on calcium (alumino)silicate hydrate chemistry under equilibrium conditions, Cem. Concr. Res. 68 (2015) 83–93, https://doi.org/10.1016/j.cemconres.2014.10.015.

[3] I.G. Richardson, The calcium silicate hydrates, Cem. Concr. Res. 38 (2008) 137–158, https://doi.org/10.1016/j.cemconres.2007.11.005.

[4] J. Li, G. Geng, R. Myers, Y.S. Yu, D. Shapiro, C. Carraro, R. Maboudian, P.J. M. Monteiro, The chemistry and structure of calcium (alumino) silicate hydrate: a study by XANES, ptychographic imaging, and wide- and small-angle scattering, Cem. Concr. Res. 115 (2019), https://doi.org/10.1016/j.cemconres.2018.09.008 (367–278).

[5] W.S. Chiang, E. Fratini, P. Baglioni, D. Liu, S.H. Chen, Microstructure determination of calcium-silicate-hydrate globules by small-angle neutron scattering, J. Phys. Chem. C 116 (2012) 5055–5061, https://doi.org/10.1021/jp300745g.

[6] R. Taylor, A. Sakdinawat, S.R. Chae, H.R. Wenk, P. Levitz, R. Sougrat, P.J. M. Monteiro, Developments in TEM Nanotomography of calcium silicate hydrate, J. Am. Ceram. Soc. 98 (2015) 2307–2312, https://doi.org/10.1111/jace.13585.

[7] A.C.A. Muller, K.L. Scrivener, A.M. Gajewicz, P.J. McDonald, Densification of C-S-H measured by 1H NMR relaxometry, J. Phys. Chem. C 117 (2013) 403–412, https://doi.org/10.1021/jp3102964.

[8] M. Wyrzykowski, P.J. McDonald, K.L. Scrivener, P. Lura, Water redistribution within the microstructure of Cementitious materials due to temperature changes studied with 1H NMR, J. Phys. Chem. C 121 (2017) 27950–27962, https://doi.org/10.1021/acs.jpcc.7b08141.

[9] G. Geng, R.N. Vasin, J. Li, M.J.A. Qomi, J. Yan, H.R. Wenk, P.J.M. Monteiro, Preferred orientation of calcium aluminosilicate hydrate induced by confined compression, Cem. Concr. Res. 113 (2018) 186–196, https://doi.org/10.1016/j.cemconres.2018.09.002.

[10] H.R. Wenk, P. Van Houtte, Texture and anisotropy, Reports Prog. Phys. (2004), https://doi.org/10.1088/0034-4885/67/8/R02.

[11] A. Morshedifard, S. Masoumi, M.J. Abdolhosseini Qomi, Nanoscale origins of creep in calcium silicate hydrates, Nat. Commun. 9 (2018) 1785, https://doi.org/10.1038/s41467-018-04174-z.

[12] P. Suwanmaneechot, A. Aili, I. Maruyama, Creep behavior of C-S-H under different drying relative humidities: interpretation of microindentation tests and sorption measurements by multi-scale analysis, Cem. Concr. Res. 132 (2020) 106036, https://doi.org/10.1016/j.cemconres.2020.106036.

[13] I. Maruyama, T. Ohkubo, T. Haji, R. Kurihara, Dynamic microstructural evolution of hardened cement paste during first drying monitored by 1H NMR relaxometry, Cem. Concr. Res. 122 (2019) 107–117, https://doi.org/10.1016/j.cemconres.2019.04.017.

[14] J. Li, W. Zhang, P.J.M. Monteiro, Preferred orientation of calcium aluminosilicate hydrate compacts: implications for creep and indentation, Cem. Concr. Res. 143 (2021) 106371, https://doi.org/10.1016/j.cemconres.2021.106371.

[15] M. Vandamme, F.-J. Ulm, Nanogranular origin of concrete creep, Proc. Natl. Acad. Sci. 106 (2009) 10552–10557, https://doi.org/10.1073/pnas.0901033106.

[16] W.A. Hunnicutt, P. Mondal, L.J. Struble, Effect of aluminum substitution in C-S-H on viscoelastic properties: stress relaxation nanoindentation, 1st Int. Conf. Gd. Challenges Constr. Mater. (2016). http://igcmat.com/papers/Hunnicutt_igcmat_2016.pdf.

[17] M. Vandamme, F.J. Ulm, Nanoindentation investigation of creep properties of calcium silicate hydrates, Cem. Concr. Res. 52 (2013) 38–52, https://doi.org/10.1016/j.cemconres.2013.05.006.

[18] N. Vandewalle, G. Lumay, O. Gerasimov, F. Ludewig, The influence of grain shape, friction and cohesion on granular compaction dynamics, Eur. Phys. J. E. 22 (2007) 241–248, https://doi.org/10.1140/epje/e2007-00031-0.

[19] A.K. Kronenberg, S.H. Kirby, J. Pinkston, Basal slip and mechanical anisotropy of biotite, J. Geophys. Res. 95 (1990) 19257–19278, https://doi.org/10.1029/jb095ib12p19257.

[20] V.M. Mares, A.K. Kronenberg, Experimental deformation of muscovite, J. Struct. Geol. 15 (1993) 1061–1075, https://doi.org/10.1016/0191-8141(93)90156-5.

[21] S.M. Mutisya, C.R. Miranda, The surface stability and morphology of tobermorite 11 Å from first principles, Appl. Surf. Sci. 444 (2018) 287–292, https://doi.org/10.1016/j.apsusc.2018.03.002.

[22] D. Tunega, A. Zaoui, Understanding of bonding and mechanical characteristics of cementitious mineral tobermorite from first principles, J. Comput. Chem. 32 (2011) 306–314, https://doi.org/10.1002/jcc.21622.

[23] F. Puertas, M. Palacios, H. Manzano, J.S. Dolado, A. Rico, J. Rodríguez, A model for the C-A-S-H gel formed in alkali-activated slag cements, J. Eur. Ceram. Soc. 31 (2011) 2043–2056, https://doi.org/10.1016/j.jeurceramsoc.2011.04.036.

[24] J. Ilavsky, Nika: software for two-dimensional data reduction, J. Appl. Crystallogr. 45 (2012) 324–328, https://doi.org/10.1107/S0021889812004037.

[25] M. Kroon, W.L. Vos, G.H. Wegdam, Structure and formation of a gel of colloidal disks, Phys. Rev. E - Stat. Physics, Plasmas, Fluids, Relat. Interdiscip. Top. 19 (1998) 887–894, https://doi.org/10.1103/PhysRevE.57.1962.

[26] B. Hammouda, A new Guinier-Porod model, J. Appl. Crystallogr. 43 (2010) 719, https://doi.org/10.1107/S0021889810015773.

[27] R.A. Vaia, W. Liu, H. Koerner, Analysis of small-angle scattering of suspensions of organically modified montmorillonite: implications to phase behavior of polymer nanocomposites, J. Polym. Sci. Part B Polym. Phys. 41 (2003) 3214–3236, https://doi.org/10.1002/polb.10698.

[28] S. Ortaboy, J. Li, G. Geng, R.J. Myers, P.J.M. Monteiro, R. Maboudian, C. Carraro, Effects of CO $_2$ and temperature on the structure and chemistry of C–(A–)S–H investigated by Raman spectroscopy, RSC Adv. 7 (2017) 48925–48933, https://doi.org/10.1039/C7RA07266J.

[29] D.W. Gardner, J. Li, S. Masoumi, M.J.A. Qomi, P.J.M. Monteiro, R. Maboudian, C. Carraro, Silicate bond characteristics in calcium-silicate-hydrates determined by high pressure Raman spectroscopy, J. Phys. Chem. C 124 (2020) 18335–18345.

[30] R.J. Kirkpartick, J.L. Yarger, P.F. McMillan, P. Yu, X. Cong, Raman spectroscopy of C-S-H, tobermorite, and jennite, Adv. Cem. Based Mater. 5 (1997) 93–99, https://doi.org/10.1016/S1065-7355(97)00001-1.

[31] L. Black, C. Breen, J. Yarwood, K. Garbev, P. Stemmermann, B. Gasharova, Structural features of C-S-H(I) and its carbonation in air-A Raman spectroscopic study. Part II: carbonated phases, J. Am. Ceram. Soc. 90 (2007) 908–917, https://doi.org/10.1111/j.1551-2916.2006.01429.x.

[32] K. Garbev, P. Stemmermann, L. Black, C. Breen, J. Yarwood, B. Gasharova, Structural features of C-S-H(I) and its carbonation in air—a Raman spectroscopic study. Part I: fresh phases, J. Am. Ceram. Soc. 90 (2007) 900–907, https://doi.org/10.1111/j.1551-2916.2006.01428.x.

[33] G. Renaudin, J. Russias, F. Leroux, C. Cau-dit-Coumes, F. Frizon, Structural characterization of C-S-H and C-A-S-H samples-part II: local environment investigated by spectroscopic analyses, J. Solid State Chem. 182 (2009) 3320–3329, https://doi.org/10.1016/j.jssc.2009.09.024.

[34] G. Geng, R.J. Myers, M.J.A. Qomi, P.J.M. Monteiro, Densification of the interlayer spacing governs the nanomechanical properties of calcium-silicate-hydrate, Sci. Rep. 7 (2017) 1–8, https://doi.org/10.1038/s41598-017-11146-8.

[35] M. Chai, J.M. Brown, Effects of static non-hydrostatic stress on the R lines of ruby single crystals, Geophys. Res. Lett. 23 (1996) 3539–3542, https://doi.org/10.1029/96GL03372.

[36] A.K. Singh, The lattice strains in a specimen (cubic system) compressed nonhydrostatically in an opposed anvil device, J. Appl. Phys. 73 (1993) 4278–4286, https://doi.org/10.1063/1.352809.

[37] A.K. Singh, C. Balasingh, The lattice strains in a specimen (hexagonal system) compressed nonhydrostatically in an opposed anvil high pressure setup, J. Appl. Phys. 75 (1994) 4956–4962, https://doi.org/10.1063/1.355786.

[38] A.M. Hofmeister, H.K. Mao, Redefinition of the mode Gruneisen parameter for polyatomic substances and thermodynamic implications, Proc. Natl. Acad. Sci. 99 (2002) 559–564. doi:https://doi.org/10.1073/pnas.241631698.

[39] Y. Sato, S.I. Akimoto, Hydrostatic compression of four corundum-type compounds: α-Al 2O3, V2O3, Cr2O 3, and α-Fe2O3, J. Appl. Phys. 50 (1979) 5285–5291, https://doi.org/10.1063/1.326625.

[40] J. Chappuis, A new model for a better understanding of the cohesion of hardened hydraulic materials, Colloids Surfaces A Physicochem. Eng. Asp. 156 (1999) 223–241, https://doi.org/10.1016/S0927-7757(99)00075-8.

[41] S.D. Palkovic, S. Yip, O. Büyüköztürk, A cohesive-frictional force field (CFFF) for colloidal calcium-silicate-hydrates, J. Mech. Phys. Solids. 109 (2017) 160–177, https://doi.org/10.1016/j.jmps.2017.08.012.

[42] A. Moshiri, D. Stefaniuk, S.K. Smith, A. Morshedifard, D.F. Rodrigues, M.J.A. Qomi, K.J. Krakowiak, Structure and morphology of calcium-silicate-hydrates cross-linked with dipodal organosilanes, Cem. Concr. Res. 133 (2020) 106076, https://doi.org/10.1016/j.cemconres.2020.106076.

[43] R.P.S. Fartaria, N. Javid, J. Sefcik, M.B. Sweatman, Simulation of scattering and phase behavior around the isotropic-nematic transition of discotic particles, J. Colloid Interface Sci. 377 (2012) 94–104, https://doi.org/10.1016/j.jcis.2012.03.046.

[44] R. Eppenga, D. Frenkel, Monte carlo study of the isotropic and nematic phases of infinitely thin hard platelets, Mol. Phys. 52 (1984) 1303–1334, https://doi.org/10.1080/00268978400101951.
[45] E.J. Tarbuck, F.K. Lutgens, Essentials of Geology 11th Edition, Earth an Introd. to Phys. Geol, 1984, https://doi.org/10.1016/0031-9201(74)90065-x.
[46] Z.P. Bažant, J.K. Kim, Creep of anisotropic clay: microplane model, J. Geotech. Eng. 112 (1986) 458–475, https://doi.org/10.1061/(ASCE)0733-9410(1986)112:4(458).
[47] J.L. Le, Z.P. Bažant, M.Z. Bazant, Unified nano-mechanics based probabilistic theory of quasibrittle and brittle structures: I. Strength, static crack growth, lifetime and scaling, J. Mech. Phys. Solids. 59 (2011) 1291–1321, https://doi.org/10.1016/j.jmps.2011.03.002.
[48] S. Strijbos, P.J. Rankin, R.J. Klein Wassink, J. Bannink, G.J. Oudemans, Stresses occurring during one-sided die compaction of powders, Powder Technol. 18 (1977) 187–200, https://doi.org/10.1016/0032-5910(77)80008-9.
[49] J. Li, W. Zhang, P.J.M. Monteiro, Synchrotron X-ray Raman scattering shows the changes of the Ca environment in C-S-H exposed to high pressure, Cem. Concr. Res. 132 (2020) 106066, https://doi.org/10.1016/j.cemconres.2020.106066.
[50] K. Ioannidou, K.J. Krakowiak, M. Bauchy, C.G. Hoover, E. Masoero, S. Yip, F.-J. Ulm, P. Levitz, R.J.-M. Pellenq, E. Del Gado, Mesoscale texture of cement hydrates, Proc. Natl. Acad. Sci. 113 (2016) 2029–2034, https://doi.org/10.1073/pnas.1520487113.